Powder bed selective laser processing (sintering / melting) of Yttrium Stabilized Zirconia using carbon-based material (TiC) as absorbance enhancer

Giovanni Urruth, Delphine Maury, Christophe Voisin, Vincent Baylac, David Grossin

Journal of the European Ceramic Society 42 (2022) 2381–2390

Contents lists available at ScienceDirect

Journal of the European Ceramic Society

journal homepage: www.elsevier.com/locate/jeurceramsoc

Powder bed selective laser processing (sintering / melting) of Yttrium Stabilized Zirconia using carbon-based material (TiC) as absorbance enhancer

Giovanni Urruth [a,b], Delphine Maury [a], Christophe Voisin [a], Vincent Baylac [c], David Grossin [b,*]

[a] Marion Technologies, Parc Technologique Delta Sud, 09340, Verniolle, France
[b] CIRIMAT, Université de Toulouse, CNRS, INP- ENSIACET, 4 Allée Émile Monso, 31432, Toulouse Cedex 4, France
[c] CIRIMAT, Université de Toulouse, CNRS, Université Toulouse 3 – Paul Sabatier, 118 Route de Narbonne, 31062, Toulouse cedex 9, France

ARTICLE INFO

Keywords:
Additive manufacturing
Selective laser sintering
Powder bed fusion
Yttrium stabilized zirconia
Titanium carbide

ABSTRACT

This study aimed to process 8 mol.% yttrium stabilized zirconia by powder bed selective laser processing, as well known as selective laser sintering / melting. Titanium carbide was used as absorbance enhancer to a Nd:YAG laser. Titanium carbide was chosen for having the lowest weight / absorbance ratio among four additive options: silicon carbide, carbon black, graphite, and titanium carbide. Several trials were performed using 0,25 wt.% of titanium carbide as absorbance enhancer of 8 mol.% yttrium stabilized zirconia, testing different laser powers, laser speeds, laser strategies, hatch distances and designs. A window of optimized parameters was identified within the study conditions, capable of manufacturing parts with high relative density. In addition, challenges and technical aspects are discussed by analyzing the observed phenomena.

1. Introduction

Additive manufacturing (AM) of ceramic materials using powder bed selective laser processing – sintering/melting (PBSLP [1]) has been targeted for its promising and challenging solutions. The possibility of fabricating complex parts on demand in a one-step process – shaping and consolidating – presents technical and economic interests [2,3]. Although PBSLP has been developed exponentially in the last decades for several ceramic materials, there are impediments [1,4] to fully control this AM method. Ceramic feedstock, independently of the chemical composition, must be tailored in terms of flowability and particle size distribution to build a well packed powder bed. Furthermore, considering the type of laser the machine is equipped, commonly a CO_2 laser ($\lambda = 10.6$ µm) or a Nd:YAG fiber laser ($\lambda = 1.065$ µm), the absorbance of some ceramic powders must be adapted to better absorb the energy emitted by the laser in question [5,6]. Most oxides have low absorbance in the wavelength issued by Nd:YAG lasers but higher absorbances in the wavelength range of CO_2 lasers [5]. Therefore sometimes, for commercial availability reasons, the absorbance range adaptation is required to adequate the ceramic powder to be processed with a specific laser.

Yttrium Stabilized Zirconia (YSZ) is largely used in high technological fields, such as aerospace [7,8] and biomedical [9,10]. However, shaping YSZ in complex designs without creating defects may be troubling and/or sometimes impossible with conventional methods. PBSLP of YSZ might be an alternative to overcome these challenges. The choice of stabilizing a specific phase of zirconia with yttrium helps to avoid or at least to reduce the possibility of any catastrophic failure during processing, due to the volume variation caused by phase transformations (up to 4%) [11]. In 2007, Bertrand et al. were the first to publish results on PBSLP of YSZ, reaching 56 % of final relative density [12]. Liu et al. studied the effect of including a pre-heating system in order to reduce cracks and control phase transformations, achieving 91 % of relative density with post-treatments [13].

Considering the low absorbance region of oxides within fiber lasers wavelengths, authors tested and demonstrated the efficiency of adding small amounts of graphite powder to enhance the energy absorption of oxides to Nd:YAG lasers [14,6]. Chang et al. enhanced the absorbance of silica powder using carbon as additive [15]. Juste et al. integrated up to 1 vol. % of graphite powder into alumina to reach 80 % of maximum absorbance, where graphite was added to the alumina slurry before spray drying [14]. Ferrage et al. added up to 2.5 wt. % of graphite into an YSZ powder to reach a maximum of 67 % of absorbance under $\lambda = 1.065$ µm, however, in this case the graphite powder was added to YSZ

* Corresponding author.
E-mail address: david.grossin@ensiacet.fr (D. Grossin).

https://doi.org/10.1016/j.jeurceramsoc.2021.12.042
Received 1 September 2021; Received in revised form 13 December 2021; Accepted 15 December 2021
Available online 17 December 2021

after spray drying [6]. Similarly, aluminum oxide powders were doped with Fe_2O_3 [16–18] or MnO_2 [18,19] to enhance its absorbance to the laser. Verga et al. proposed a novel approach to the strategy used by Juste [14] and studied the pyrolysis of the spray drying binder as carbon source to enhance the absorbance of the alumina-toughened zirconia particles [20].

Considering the commercial availability of PBSLP machines equipped with Nd:YAG lasers, this study aimed to obtain consolidated parts from PBSLP of YSZ using a carbon-based material as absorbance enhancer to a Nd:YAG laser. A preliminary study compared the efficiency of graphite, carbon black (CB), titanium carbide (TiC) and silicon carbide (SiC) as alternatives to be added into YSZ, to evaluate the lowest vol.% / absorbance enhancement ratio. These alternatives were added into an 8% Yttrium Stabilized Zirconia (8YSZ) powder, stabilized with a cubic phase structure. Once chosen, the best additive among the four will be tested under several laser processing conditions. Dense parts will be manufactured by PBSLP by varying laser parameters to seek understanding of the occurring phenomena. Laser speed (mm/s), laser power (W), hatch distance (μm) and laser strategy were the main control parameters used in this study.

The Evaluation of PBSLP of 8YSZ face the variation of laser parameters during processing is guided by key points, like the processing limits of energy to obtain a solid part, the influence of the laser parameters and the influence of the number of layers on the final density.

2. Materials and methods

8YSZ powder was synthesized with a combustion reaction [21]. First step, zirconium nitrate – $Zr(NO_3)_4{\cdot}5H_2O$ (*Treibacher Industrie AG, Austria*), urea – CH_4N_2O (*BASF, Germany*) and yttrium oxide – Y_2O_3 (*Marion Technologies, France*) were dissolved separately into deionized water and nitric acid (HNO_3). After mixing the three dissolved components into a final solution, thermal treatments were performed to synthesize 8YSZ powder. The molar composition was verified posteriorly by inductively coupled plasma atomic emission spectroscopy (ICP-AES) using a Shimadzu ICPE-9820. 8YSZ powder was then dry-grinded for 1 h with zirconia grinding bodies (Ø = 2 cm) and wet milled for 30 h, in ethanol, using zirconia grinding balls (Ø = 1.1 μm). 8YSZ wet milling suspension was dried at 100 °C for 12 h. Wet milled 8YSZ dried powder was dispersed in deionized water in presence of an organic binder, under continuous agitation. This suspension was spray dried using a Niro atomizer. 8YSZ spray dried particles were, at first, debinded at 500 °C for a few hours to remove the reminiscent organic binder. Secondly, the particles were treated at 1200 °C for 2 h to promote cohesion and to avoid the spheres to break during transportation. The flowability of the spray dried particles was measured using a tap density method and the Carr Index was calculated [22]. Particle size distribution (PSD) was verified by laser granulometry using a Malvern Instruments Mastersizer 2000 coupled with a hydro 2000s module and x-ray diffraction (XRD) analysis were performed using a Inel CPS 120, Cu-Kα (1.54 Å), after each step of the tailoring method and after processing.

The alternative additives for enhancing the absorbance of 8YSZ are SiC (*Marion Technologies, France*), TiC (*Marion Technologies, France*), carbon black - CB (*Alfa Aesar, USA*) and graphite (*Alfa Aesar, USA*), with the respective PSD (d_{50}) of 550 nm, 850 nm, 1.7 μm and 1.5 μm. All mixtures were made using a WAB Turbula® shaker mixer without any grinding body for 24 h. The absorbance enhancement method was evaluated using a Perkin-Elmer Lambda Series / UVCSS, scanning the reflectance of all samples in the wavelength range of 700–1300 nm. The nearest points to λ = 1065 nm were picked as reference to simulate the absorbance of a Nd:YAG laser and to make a comparison between the additives.

A 3D Systems ProX 200 was used to perform the PBSLP of 8YSZ. Laser parameters were tested in ranges: laser power from 30 W to 96 W, laser speed from 8 mm/s to 80 mm/s, hatch distance from 35 μm to 85 μm, laser focus ranging from – 0.5 mm to +1.5 mm (platform shift in the Z direction, in relation to the Z coordinate of the layer being processed). The variation of the laser focus implies the variation of the laser spot size. Layer thickness of 100 μm, spot size of 75 μm, compaction rate of 300 % and air atmosphere inside the chamber were kept constant. The compaction rate was described by Ferrage et al. [6] as the thickness ratio added to the layer thickness before compaction of the roller. The powder bed was spread out by a roller that passed over the powder in two steps for each layer: Step 1) spread the powder over the building platform; and step 2) the roller comes back to make the powder bed compaction. The building platforms were 14cm × 14cm plates made of aluminum. Designed samples consisted of 0.8cm × 0.8cm x 0.3 cm cuboids, spaced by 0.4 cm and 1.4cm × 1.4cm x 0.4 cm cuboids, spaced by 2 cm. At least 300 samples were processed.

Laser energy density has been used to analyze results obtained by PBSLP [23–25]. Other studies recently started to evaluate the effects of laser strategy [26,27]. The strategy of varying different laser parameters to find the optimal processing conditions of this carbon-based enhanced 8YSZ is complex. This complexity was mainly focused on the laser energy density as reference to analyze and compare the obtained results. Laser power (P), laser speed (ν), hatch distance (h) and layer thickness (t) can be combined to calculate the laser energy density (E_d) in a proposed volume (Eq. (1)).

$$E_d = \frac{P_{laser}}{v_{scan}.h_{space}.t_{layer}} \left[\frac{J}{mm^3}\right] \quad (1)$$

In addition, different laser strategies were tested to observe their effect during processing. Linear strategies scan parallel lines spaced by the hatch distance (Fig. 1(a) and (c)). A subsequent layer (layer n + 1) usually twists the scanning direction by a predefined degree, i. e., rotates from a chosen angle: 90 °, 30 °, 45 °, etc. (Fig. 1(a) for 90 °). Concentric strategies scan concentric shapes throughout the surface of the part and two directions may be chosen: starting by the exterior and to finish in the center of the part (exterior/interior), and the other way around (Fig. 1 (b)). Hexagonal strategy is part of a group described as “island” strategy, described elsewhere [1]. A list of references and details to all laser strategies used in this study is presented at Table 1.

The densities of the manufactured parts were measured by Archimedes’ principle using a Mettler Toledo AG104 balance and a density determination kit suitable for this specific model. Measurements of dry mass, wet mass and submerged mass were taken for the calculations. Processed samples were embedded into a transparent epoxy resin and polished with a Metkon Forcipol 102, using SiC paper grinding discs with grit size varying from P120 to P2500 and water-based diamond suspensions of 6 μm and 1 μm. A Zeiss EVO MA15 scanning electron microscope (SEM) was used to observe the samples morphology in different situations, also as complement to the observations made using a standard optical microscope. Vickers micro-hardness measurements were performed using a Tukon 1202, with a 100 g of load and a dwell time of 10 s. The software Ellistat was used to process the processing data to find out the correlations between the tested parameters and to compare their individual contribution to the final density of the parts.

3. Results

3.1. 8YSZ powder tailoring

The proportions of all elements were calculated to have the molar stoichiometry of $Zr_{0,84}Y_{0,16}O_{1,92}$., molar composition that was checked and confirmed after synthesis (8% yttrium stabilized zirconia – cubic phase).

Three stages (after synthesis, wet milled and spray dried) of the tailoring process were characterized by XRD, SEM and laser granulometry (three times each sample) to confirm their morphology, PSD and that no phase transformation took place during the milling process (Figs. 2–4). The whole tailoring process did not cause any variation to

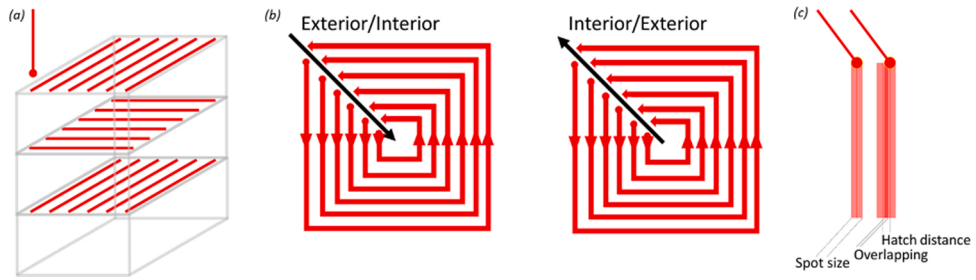

Fig. 1. Scheme illustrating the successive laser scanning over different layers, for a linear laser scanning strategy with 90 ° of rotation (a), for concentric strategies (b) and the hatch distance (c).

Table 1
Description of the laser strategies and respective references used in this study.

Reference	Laser strategy (Fig. 1)	Base angle (°)	Rotation (°)	Method	Details
N30	Linear	30	60	–	–
N45	Linear	45	90	–	–
N90	Linear	90	180	–	–
N90P1	Linear	90	180	–	Made on plate 1
N90P2	Linear	90	180	–	Made on plate 2
N90P5	Linear	90	180	–	Made on plate 5
C1	Concentric	0	0	Internal/ External	Contours
C2	Concentric	0	0	External/ Internal	Contours
C3	Concentric	0	0	Edge to edge	Contours
C4	Concentric	0	0	Internal/ External	Central Line
C6	Concentric	0	0	Edge to edge	Central Line
C7	Concentric	0	0	Internal/ External	Neutral Fiber
C9	Concentric	0	0	Edge to edge	Neutral Fiber
C10	Concentric	0	0	External/ Internal	Neutral Fiber
F1	Linear	90	180	Focus positive*	+0.5 mm
F2	Linear	90	180	Focus positive	+1 mm
F3	Linear	90	180	Focus positive	+1.5 mm
F4	Linear	90	180	Focus negative*	−0.5 mm
H	Hexagonal	90	180	Not progressive	10000 µm hexagons

* Focuses with positive numbers are above the zero at the surface of the platform.

the cubic phase (JCPDS No. 49-1642) [28], indexed in Fig. 2. After the combustion reaction, the agglomerates formed presented irregular shaped porous structures (Fig. 3(a)). A finer morphology was obtained after wet milling (Fig. 3(b)), with a $d_{50} = 1.1$ µm ± 0.05 (Fig. 4). Spray dried particles presented a homogenous spherical pattern (Fig. 3(c)) and a $d_{50} = 34.7$ µm ± 0.14 (Fig. 4).

3.2. Absorbance enhancement

TiC, SiC, CB and graphite were selected as additive alternatives to enhance the absorbance of the 8YSZ powder to the laser. These additives presented a PSD (d50) of 850 nm, 550 nm, 1.7 µm and 8 µm, respectively. The absorbance of the additives (pure) to the laser were 82 %, 78 %, 80 % and 90 %. Two samples were prepared with each alternative additive with the proportions of 0.25 wt. % and 0.75 wt.%. The objective

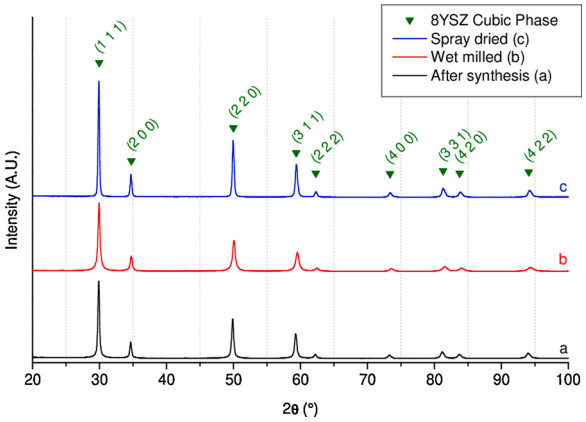

Fig. 2. X-ray diffractograms for the synthesized 8YSZ powder: after synthesis (a), wet milling (b) and spray drying (c) steps. 8YSZ cubic phase is indexed.

was to enhance the absorbance of 8YSZ powder from 4.5 % to near 60 % at a wavelength of approximately 1.065 µm, using the minimum amount of additive possible (Table 2). The sample containing 0.25 wt.% of TiC was selected as the one with the minimal weight/absorbance ratio to approach the target of 60 %. The presence of TiC in 8YSZ powder is discussed in chapter 4.

The flowability of 8YSZ +0.25 wt.% TiC was measured to assure a good particle flow during the layer formation in PBSLP. The flowability of a powder is usually considered good to excellent with a Carr Index under 15 and considered bad when over 35. The final Carr Index obtained to 8YSZ +0.25 wt.% TiC was 17.6 ± 0.4, similar to other researches performed with YSZ and ceramic powders [6,14].

3.3. Powder bed selective laser processing

In Fig. 5, initial results are summarized qualitatively when crossing a laser power range from 30 W to 57 W against a laser speed range from 8 mm/s to 80 mm/s (plate 1), for a N90 laser strategy and a hatch distance of 50 µm. Plate 1 was designed to find where the laser conditions would be sufficient to interact with 8YSZ +0.25 wt.% TiC and consolidate particles (metal/ceramic interface) that were attached to the platform. In other word, where it begins to interact with the aluminum platform to yield adhesion, to find the minimal energy required to form a consolidated part and to understand how this energy should be delivered by the laser, i.e., the correlation between the laser power and laser speed. The first interaction to be observed is illustrated at Fig. 5(a), where there is adhesion between melted particles of 8YSZ and the aluminum platform. In Fig. 5(b), the formation of a macroporous structure, where melted drops are observed, evidence interconnected particles touching each other in small edges of sintering (necks). In Fig. 5(c), a consolidated structure is presented, and its parameters were the best processing conditions of plate 1 (57 W and 32 mm/s). However, in Fig. 5(d) and (e), two different impacts of exposing samples to an excess of energy are

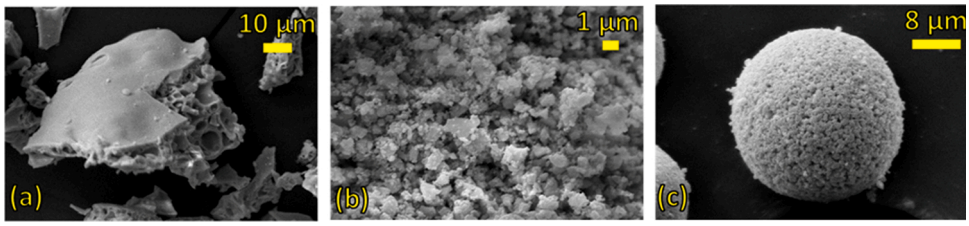

Fig. 3. SEM images of the 8YSZ powder: (a) after synthesis, (b) after wet milling and (c) after spray drying.

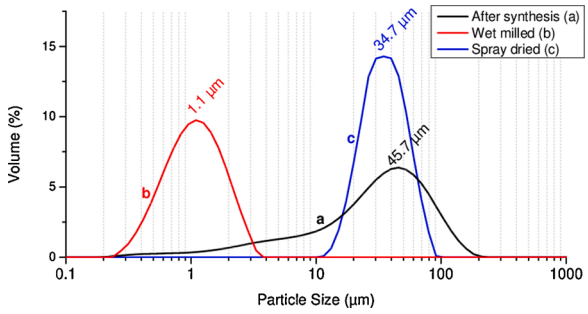

Fig. 4. Particle size distribution (d50 in evidence) of the 8YSZ particles: after synthesis (a), wet milling (b) and spray drying (c) steps.

Table 2
Absorbance of 8YSZ mixed with SiC, Graphite, Carbon Black and TiC, in two different compositions of 0.25 and 0.75 wt.%, under a wavelength of 1.065 µm. Pure 8YSZ presented 4.5 % of absorbance.

Powder + additive	Absorbance* at 1065 nm (%)	
	0.25 wt.% of additive	0.75 wt.% of additive
8YSZ + SiC	18.9	29.5
8YSZ + Graphite	32.5	43.4
8YSZ + Carbon Black	54.9	66.6
8YSZ + TiC	**57.4**	67.8

* Pure 8YSZ presented 4.5 % of absorbance at 1065 nm.

presented. In case of Fig. 5(d), there is degradation of the platform and powder that precludes the consolidation of a solid over the platform. And in Fig. 5(e), the excess of energy is less important that the precedent, but enough to cause dimensional instability of the processed part (designed in a cubic shape).

In Fig. 6, results are shown for a laser power range from 72 W to 96 W that was tested against a laser speed range from 60 mm/s to 70 mm/s (Plate 2), for a N90 laser strategy and a hatch distance of 50 µm. Analogously, a chart is presented to illustrate the density evolution through the parameter combinations. Plate 2 was designed to find the upper limit of energy to process 8YSZ, where the parameters would start to degrade the samples. The parameter combinations in plate 2 evidence an increase in density towards higher laser power values. In addition, there is a slight tendency for higher densities towards a laser speed of 60 mm/s compared to that of 70 mm/s. The objective of the combination of parameters for plate 2 was to identify the top limit of laser energy density for that specific window of processing. Upon varying the laser power and laser speed towards higher levels of laser energy density, certain dimensional integrity defects on the surface of samples are visible at a laser power of 93 W. In the subsequent layer of samples, tested for 96 W of power, the samples were degraded from the first layers, damaging the platform.

All the processed and consolidated cuboids of dimensions 0.8cm × 0.8cm x 0.3 cm had the density measured by the Archimedes' method. In Fig. 7 are presented the measured densities of samples processed with similar conditions, plotting density (g/cm^3) x laser energy density (J/mm^3).

In Fig. 8, the densities of cubic samples with two design volumes of 0.512 cm^3 (0.8cm × 0.8cm x 0.8 cm) and 2.744 cm^3 (1.4cm × 1.4cm x 1.4 cm) are crossed against laser energy density. Two zones are formed, distinguished in blue and red, representing the smaller and the bigger parts, respectively.

All the collected data used to plot both Figs. 7 and 8 were refined to 168 samples (disregarding samples presenting very high residual, which represents the gap between the observed and the predicted value) and used to create a linear regression to analyse the possible correlations among the following parameters for the final density (dependent variable) of the parts (R^2 = 96.6 %): laser power, laser speed, laser strategy, design (size) of the part, mass of the samples and hatch distance (independent variables). The results are shown in Table 3.

To check the intrinsic effect of the hatch distance, a sequence line of 10 samples was made by maintaining a laser speed of 60 mm/s, laser

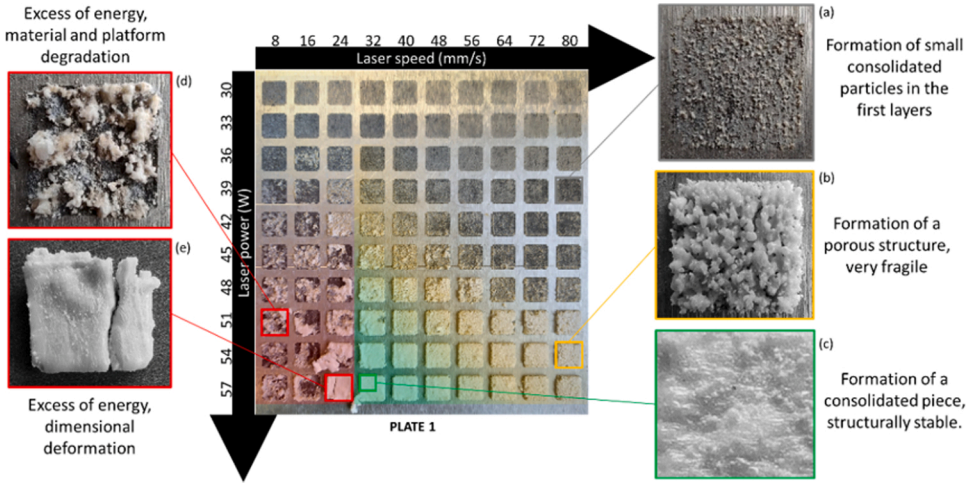

Fig. 5. Details of the manufactured plate n° 1. 100 cuboids of dimensions 0.8 × 0.8 × 0.3 cm combining a laser speed ranging from 8 to 80 mm/s and a laser power ranging from 30 W to 57 W. Three zones are highlighted: Red – excess energy; Yellow – lack of energy; and Green – highest densifications among the tested parameters. (a) Beginning of adherence between melted particles and the platform but no subsequent adherence of ceramic particles; (b) the macroporous structure formed by melted material and adequately adherent to the platform; (c) consolidated sample with a density of 5.51 g/cm^3; (d) excess energy degrading the material and platform; (e) excess energy causing dimensional variation. (For interpretation of the references to colour in this figure legend, the reader is referred to the web version of this article).

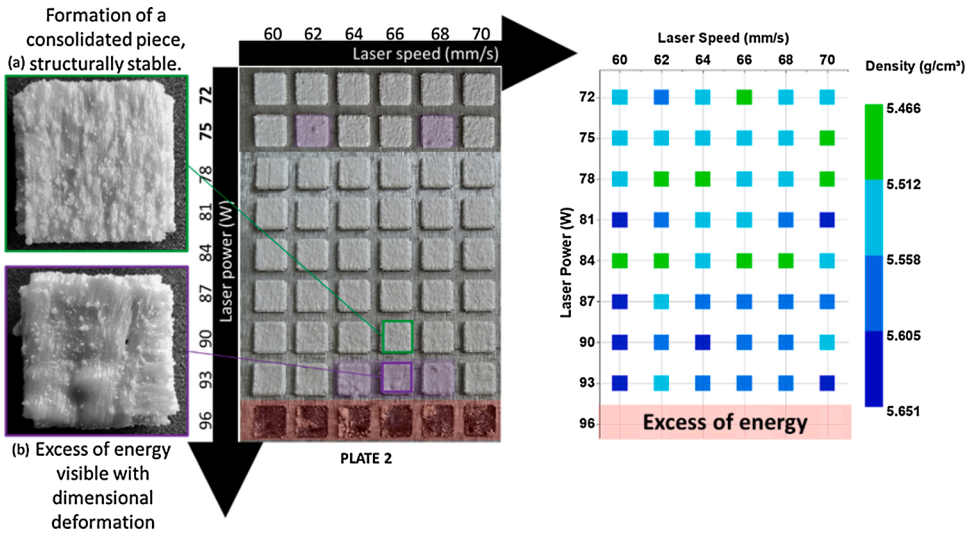

Fig. 6. Details of the manufactured plate number 2. 54 cuboids with dimensions of 0.8 × 0.8 × 0.3 cm combining a laser speed ranging from 60 to 70 mm/s and a laser power ranging from 72 W to 96 W. One Red zone is highlighted: excess energy degrading the platform. A chart displaying the corresponding density of each sample is displayed. (a) A sample without dimensional deformation; (b) example of dimensional degradation. (For interpretation of the references to colour in this figure legend, the reader is referred to the web version of this article).

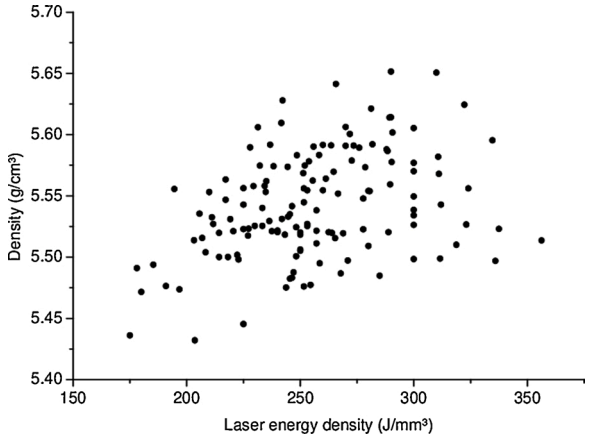

Fig. 7. Density (g/cm^3) vs laser energy density (J/mm^3), with a dispersion for all cuboids with dimensions of 0.8 × 0.8 × 0.3 cm of 8YSZ +0.25 wt.% TiC samples fabricated by PBSLP.

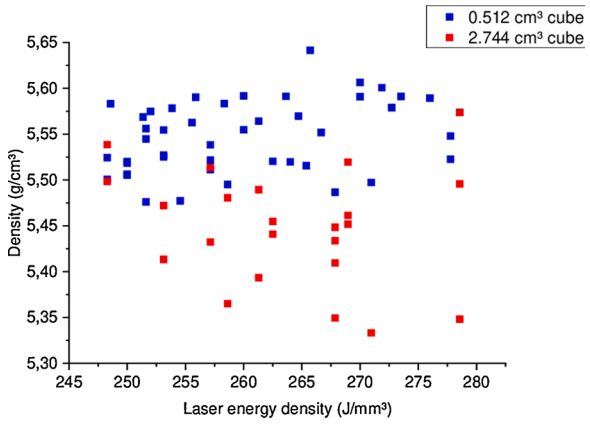

Fig. 8. Density (g/cm^3) vs laser energy density (J/mm^3), with a colour-mapping for two different designs (0.512 and 2.744 cm^3 cuboids), of 8YSZ +0.25 wt.% TiC samples obtained by PBSLP.

power of 75 W, and laser strategy at N90 but varying the hatch distance from 35 μm to 85 μm. As a result, a relative density variation of approximately 1.6 % is observed (Fig. 9). However, the sample with a hatch distance of 35 μm presented excess energy and did not consolidate (similar to Fig. 5(d)). The parts with relatively large hatch distances yielded relatively low density. A linear equation expressing the evolution of density against the lowering of hatch distance from 40 μm to 85 μm was presented. This kind of isolated analysis may also be interpreted from the result of changing the energy density, which cannot be maintained in a fixed value (possibility of analyzing the effect of varying the hatch distance at the same energy density) without changing other parameters to balance the energy density values.

Table 3
Contributions of the laser control parameters set by a linear regression algorithm within the processing windows displayed in Figs. 7 and 8.

Data/parameter	Contribution to the final density (%)**
Design (size)	76,5
Laser power	5,5
Laser strategy	2,8
Hatch distance	2,7
Laser speed	1,7

** The contribution sums up to 100 % when added to the terms of mass (g) and residual.

Additionally, maintaining a laser speed of 60 mm/s, a laser power of 75 W, and a hatch distance of 50 μm but varying the laser strategy, a variation of 1.48 % in density may be observed (Fig. 10). The results are sorted from the smallest to highest density, from left to right. Strategies F4, N90P1, N90P5, C9, and N90P2 have relatively high densities. Linear laser scanning strategies tend to present higher densities than concentric strategies.

Samples with the same shape, similar laser energy density but different laser strategies were polished and had their surface tested for Vickers micro-hardness indentation (HV0.1). The range within 1550 Hv to 1930 Hv was measured, and the results were mainly consistent with those of other reported data on processed cubic 8YSZ [29] (Fig. 11). However, some results presented unusual high hardness values (above 1900 Hv) for a cubic zirconia phase and should be observed with care. Owing to the presence of cracks, all the measurements were aimed at obtaining smooth and well consolidated regions of the surface.

The used laser strategy on the microstructure of the manufactured parts can be observed and correlated using an optical microscope. The surfaces of consolidated samples obtained using the concentric strategy were analyzed. Fig. 12 displays the bottom-left corner of a C2 strategy, where the laser changes direction, forming the square designed shape. To properly observe the impact of the laser direction in the microstructure of an N45 strategy, samples were polished slightly diagonally.

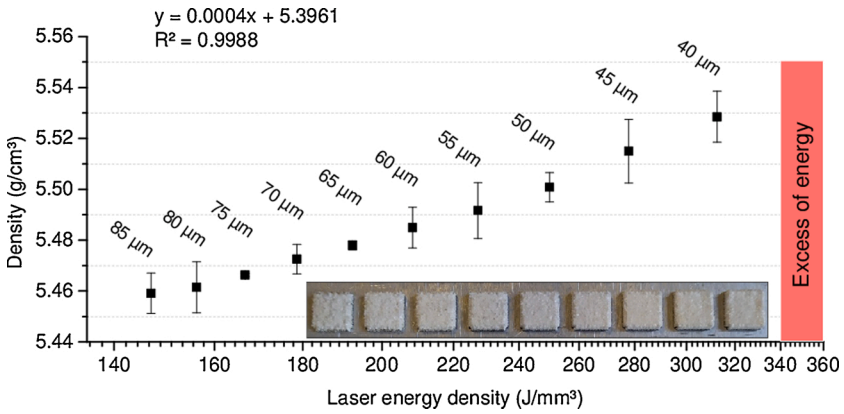

Fig. 9. Measured density (g/cm^3) vs laser energy density (J/mm^3) for 8YSZ +0.25 wt.% TiC samples processed by PBSLP with laser speed = 60 mm/s, laser power = 75 W and hatch distance varying from 40 µm to 85 µm. Hatch distance is a factor that influences the laser energy density as showed in Eq. (1).

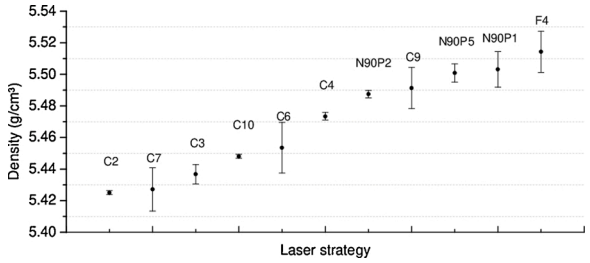

Fig. 10. Density (g/cm^3) x laser strategy for 8YSZ +0.25 wt.% TiC samples processed by PBSLP with laser speed = 60 mm/s, laser power = 75 W and hatch distance = 50 µm.

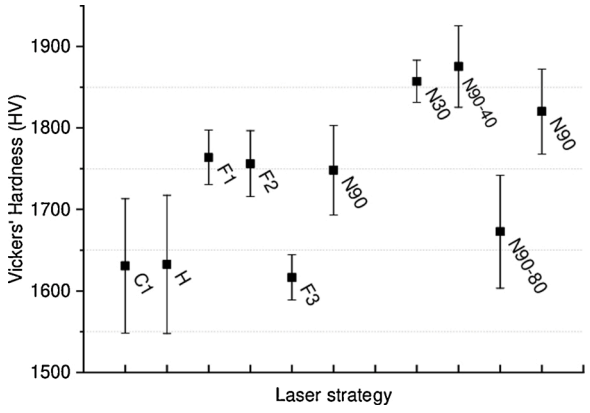

Fig. 11. Vickers' hardness (HV) x laser strategy for 8YSZ +0.25 wt.% TiC samples processed by PBSLP with laser speed = 60 mm/s, laser power = 75 W and hatch distances of 50 µm for all samples but N90-40 and N90-80 that have 40 µm and 80 µm, respectively.

As illustrated in and correlated to the scheme in Fig. 13, an example of a transition zone between a layer at 0 ° and a subsequent layer at 45 ° is presented.Fig. 14 shows evidence of the achievement of a relatively high density in the surrounding regions of a sample, causing a different shrinkage rate between the surroundings and the core of the part. In this example, this phenomenon caused a dimensional deformation that resembled a mushroom-like format.

Fig. 15 shows an example of the dense part processed using some of the optimal parameters presented in this study. It was processed using a N90 laser strategy, a laser power of 75 W, a laser speed of 60 mm/s, and a hatch distance of 70 µm. It presented 97 % of relative density.

Fig. 16 shows the microstructure of a sample processed with a N90

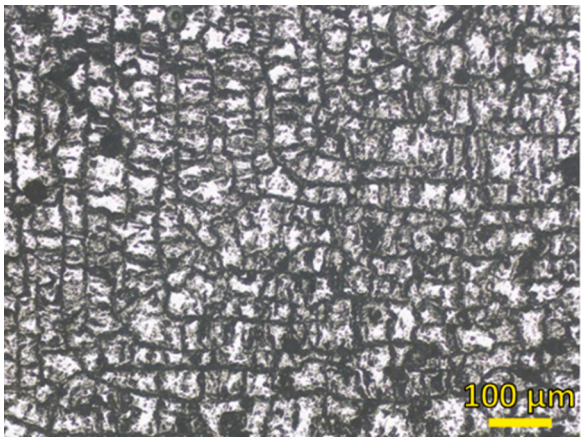

Fig. 12. Microstructure of a 8YSZ +0.25 wt.% TiC sample processed with a concentric laser strategy by optical microscopy (100x).

after a fracture. Intra and interlayer cracks are visible after the fracture, alongside with the localized cleavage planes, signs for a rapid brittle rupture.

4. Discussions

4.1. Tailoring 8YSZ powder to PBSLP

To be spray dried, 8YSZ average particle size (d_{50}) must be adapted to the spray drying operating conditions. In this work, the optimal particle size (d_{50}) set to achieve before spray drying was near 1 µm. After combustion synthesis, the powder aggregates and particulates do not present yet the optimal morphology to be spray dried and to reduce the average particle size (d_{50}), two steps were taken: dry grinding and wet milling [30]. The step of dry grinding breaks the biggest agglomerates and porous particulates formed during synthesis and wet milling separates the reminiscent and smaller aggregates (Figs. 3 and 4).

Fluidity/viscosity of the mixture directly influences the manufactured spheres during spray drying. The process temperatures were regulated to guarantee a full vaporization of water when the solution passes throughout the turbine, considering that the water drying speed is directly connected to the temperature on top of the chamber, where the turbine is located, and might also influence the hollowness of the final spheres [31].

As TiC was added to 8YSZ spray dried powder once it was manufactured, the method to homogenize the mixture must not damage the spherical particles. Breaking or substantially damaging the spherical

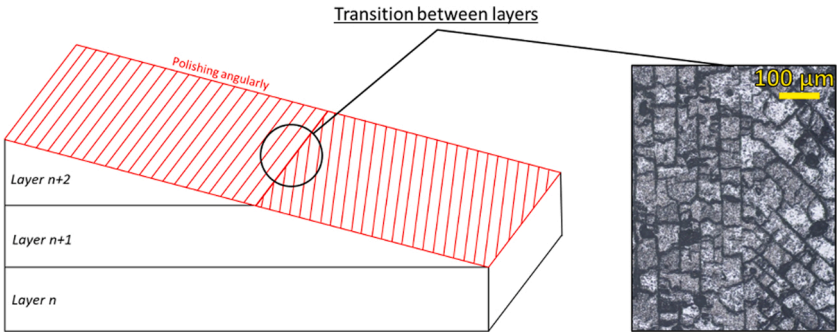

Fig. 13. Microstructure of a 8YSZ +0.25 wt.% TiC sample processed with a linear laser strategy with 45 ° of rotation by optical microscopy (100x).

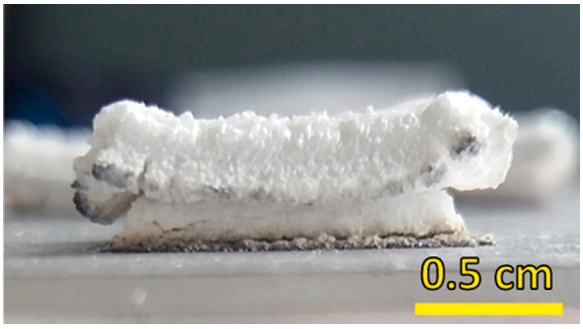

Fig. 14. Lateral perspective of a cuboid of 1.4 × 1.4 × 0.4 cm displaying mushroom-like deformation caused by overheating the upper surrounding regions of the part.

particles would imply in flowability losses, by creating new mechanical resistances between particles in movement. This risk may also be lowered by the thermal treatment to near sintering temperature that was set to promote cohesion inside the spheres.

PBSLP is performed in a chamber containing oxygen, consequently provoking the inserted TiC to oxidize during heating and forming TiO_2. The effects of small amount of TiO_2 in the YSZ structure may be beneficial to enhance the densification [32,33], ionic conductivity [34] and the sintering behavior [35], but complementary studies are required to verify those in this work.

4.2. Influence of PBSLP parameters

In Fig. 5, the variation of density considering all combinations of factors presented two extreme and opposite behaviors: 1) the points with too little energy to sinter/melt ceramic particles (Fig. 5(a)), where the laser conditions do not allow for the formation and sintering (consolidation by diffusion) of subsequent layers, i.e., after the first layers that interact with the metallic platform with a ceramic/metal interface, the energy is insufficient for the interaction of particles within the ceramic/ceramic interfaces; 2) Points where there was too much energy that the sample (Fig. 5(e)) or the platform degraded (Fig. 5(d)). In between those extremes is a window of parameters that yields the suitable amount of

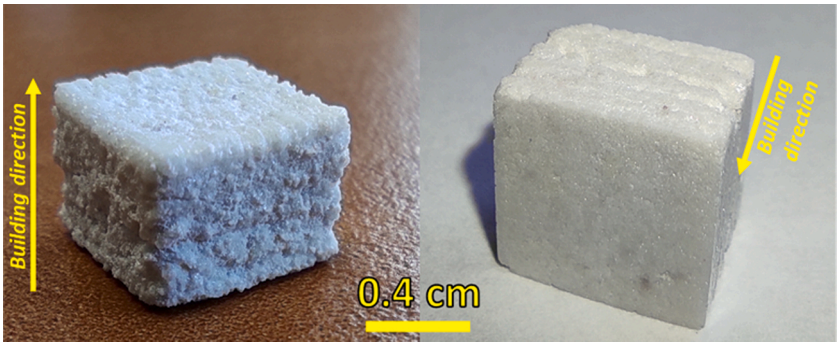

Fig. 15. 0.8cm × 0.8cm x 0.7 cm cuboid processed by PBSLP using parameters in the studied optimal window. (a) after PBSLP; (b) lateral view of the polished top surface.

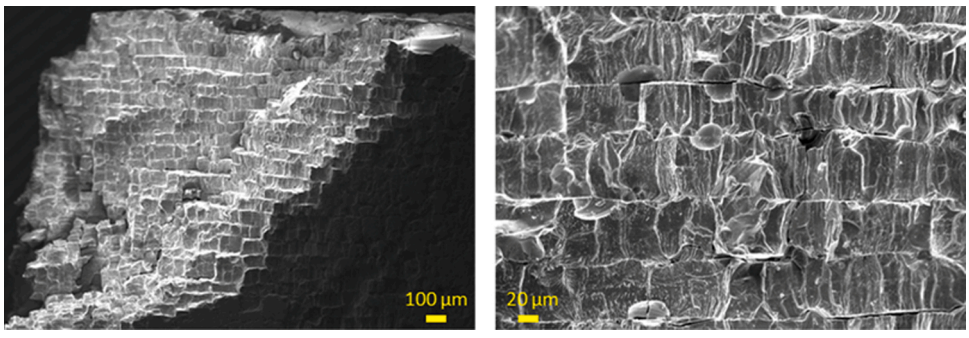

Fig. 16. Cracks and fracture planes on a sample processed with a N90 laser strategy.

energy for the fabrication of a dimensionally stable and dense part.

Four different zones in plate 1, represented by grey, yellow, green and red colors are observed. The grey zone is where the laser conditions were sufficient to interact with 8YSZ +0.25 wt.% TiC and consolidate particles (metal/ceramic interface) that were attached to the platform (Fig. 5(a)). Consequently, only some particles were attached to the platform after cleaning, and the energy was insufficient to cause ceramic/ceramic interactions to form edges of sintering (necks) and build a solid structure. On the yellow zone (Fig. 5(b)), the macroporous structures are brittle and cannot be handled or detached by the platform in one part. In the green zone, the presented parts are consolidated and dense (Fig. 5(c)), indicating that the zone at approximately 32 mm/s and 57 W (356 J/mm^3) is where the conditions of processing 8YSZ + 0,25 wt.% TiC should be explored to refine the optimal conditions. Finally, the red zone is where the laser conditions present excess energy. The excess may create defects ranging from degradation of the platform and overheating of the powder, forming degradations from a hole with melted ceramic/metal phases (Fig. 5(d)) to dimensional deformation of the processed part (Fig. 5(e)).

The presented data in Fig. 7 evidence a density zone that is correlated to the combination of laser power, laser speed, and hatch distances, which varies the laser energy density from approximately 175–355 J/mm^3. The highest densities (approximately 5.85 g/cm^3) were obtained via relatively high laser speeds and laser power. This value is based on the densities obtained in a similar study conducted by Ferrage [6] (5.77 g/cm^3).

In Fig. 9, the effect of varying the hatch distance, which consequently affects the overlapping and laser energy density, for the same laser strategy, power, and speed, is shown. The final temperature reached by samples with higher hatch distances is relatively low, resulting in relatively less dense parts. By varying the hatch distance, the overlapping region of each scan changes. As the reliable in situ verification of the temperature during PBSLP is overly complex, two main phenomena may be happening. 1) When overlapping takes place, the area exposed for the second time supposedly melts and solidifies again; and 2) overlapping may allow the area scanned for the second time to finally melt, considering that the first scan was insufficient to reach the melting point. To corroborate these theories, simulation studies have been conducted to analyze the impact of hatch distance and overlapping and similar conclusions have been drawn [36,37].

In Fig. 14, heat flow and diffusion occur during the layer by layer construction of a part, first, from the top (laser) to bottom (platform), through the already processed layers. Secondly, after having diffused throughout all ceramic material, the heat diffuses via the aluminum platform. Understanding the difference between the thermal conductivity in a ceramic zone and that in the transition ceramic/metallic zone is also essential to more optimized dimensional stability during PBSLP [38]. The surroundings of a cuboid that is being processed remains made of raw powder (non-processed), which possesses exceptionally low thermal conductivity. This may create an insulating barrier around the processed parts, preventing heat flow by conduction from all directions but the bottom (platform). This indicates that the surroundings of a sample may have less capacity for evacuating the heat after the laser has scanned, consequently overheating the region.

The insulating barrier effect described may not be as important when a non-oxidizing atmosphere is used inside the chamber of the PBSLP machine. In other words, in a chamber lacking oxygen, TiC particles are not oxidized into TiO_2. The absorbance and thermal conductivity of TiC could have an influence on the local properties of each layer.

Within the parameters tested in this study, the minimum and the maximum laser energy density that resulted in a solid part were, respectively, 147 J/mm^3 and 475 J/mm^3. The former with laser power = 75 W, laser speed = 60 mm/s and hatch distance = 85 μm, presenting a final density of 5.46 g/cm^3 and the latter with laser power = 57 W, laser speed = 24 mm/s and hatch distance = 50 μm, presenting a final density of 5.60 g/cm^3. It is important to clarify that might exist other windows of processing to the same material, which may possibly have a similar or even better result. In addition, controlling the laser parameters and strategy, one may reach similar energy density by choosing totally different combinations that those performed in this study. As well as using different laser parameters and strategies throughout a same building platform, to adapt to a higher heat diffusion in the beginning by the proximity to the aluminum platform and lower heat diffusion for parts with progressively more layers. Once the heat diffusion behavior is well stablished when samples are exposed to the laser during PBSLP, one may control the laser parameters and strategies to maintain the same levels of heat diffusion.

Analyzing the results presented in Figs. 7, 8 and Table 3, although the window of laser energy density shown on those figures is limited to a maximum of 355 J/mm^3, it is possible to state that higher densities are achieved when combining higher laser power and speed rather than combining lower laser power and speed, even though those combinations reach similar amount of laser energy density. There is evidence that the effect of rising laser power is more beneficial (around 3x) for the final density than the rise of laser speed, for a given laser energy density, among the studied parameters for 8YSZ + 0.25 % TiC. No combination of parameters seems to be effective to reduce or eliminate the microstructural cracks after processing. As presented in Fig. 9, by varying the hatch distance from 35 μm to 85 μm, it is noticeable that controlling the overlapping between successive laser lines has an important effect on the final density.

The most influent parameter (on the final density of the samples) among the ones controlled in this study, in the processing windows used, is the design of the part (size). It presents by far (Table 3), almost 14x more than laser power, the biggest contribution to the final density of the parts.

Comparing the contributions displayed in Table 3, laser strategy has a similar impact on the final density than hatch distance and 1% more than the laser speed, within the studied windows of processing. The presented evidence in Figs. 12 and 13 shows that the laser strategy has an impact on the microstructure and that this impact has a “fingerprint” related to the conditions of each specific layer. However, it is not possible to understand how the microstructure is organized between layers (building direction). Further investigations may be required (MicroCT-Scan, for example). Extending the analysis to Fig. 11, the laser strategy has an important impact in the resultant micro-hardness as well.

Within the laser strategy parameters tested in this study, it is not clear the complete impact of this factor on the quality of the samples. Influence on the hardness, on the final density and on the microstructure observed after processing, when varying the laser strategy. However, more samples must be processed using the same set of laser parameters and varying only the laser strategy to perfectionate the analysis. Other laser strategies, for example hexagonal patterns, may be as well optimized to manufactured dense zirconia parts. Similar results were obtained for zirconia + graphite combination [6].

Qualitatively, analyzing the example displayed in Fig. 14, it is possible to infer that the height (nº of layers) might have an influence firstly on the heat flow from the top of the part to its bottom, and secondly through the platform. More layers, more ceramic material that heat must pass to flow by the platform. This influence is directly connected to the time gap between two layers are built. For a 14cm × 14cm surface platform with up to 100 samples, considering the parameters used in this study, it is common to have up to 60 min. between each layer. Which means that each sample has 60 min to cool down and evacuate the heat through the previous built layers of pure ceramic and through the platform. However, some designs may include only a few or even a single sample to be built, reducing the time gap between layers to a few seconds. Although qualitatively reasonable, the magnitude of this temperature cooling range could not be measured with certitude with the used setup, requiring further investigations.

The evidence that the shape (or size) of the designed part has

influence on the final density, is shown in Fig. 8, where final density is crossed against laser energy density and shows two main regions. Parts with design dimensions 0.512 cm^3 tend to have higher densities than parts with a design dimension of 2.744 cm^3 (volume approximately 5.36x larger). This difference may be explained by the longer average course of the laser to scan to complete each layer. Longer the laser pointer takes to return to a certain region of the surface, longer this specific region evacuates heat. Consequently, all the subsequent passages of the laser near that specific region of the surface will have lower mean temperature when compared to a smaller sample. This effect has also an important role when analyzed in a different layer position. Higher the sample, longer takes to diffuse and higher the temperature remains, but this has a different effect for different designs mainly because bigger samples have more core surface that is not surrounded by insulator powder (sample borders).

The option of scanning the same layer, or laser path, more than once was considered at first for this study to better control the final density of the parts. But this addition would have added complexity to this analysis, and it was left for a next step of the study. However, Navarrete-Segado et al. have tested this condition in their process to PBSLP of calcium-phosphate-based powders [39].

5. Conclusions

8YSZ was synthesized by combustion route and tailored to PBSLP. The process consisted of preparing the powder for spray drying and adapting its absorbance for a Nd:YAG laser, using 0.25 wt.% of TiC as absorbance enhancer additive. PBSLP tests were performed varying laser power, laser speed, laser strategy, hatch distance and design. The final parts were analyzed in terms of density to correlate their characteristics to the corresponding set of parameters used during PBSLP. It is possible to state that the laser power, laser speed, laser strategy and the hatch distance influence directly the final density of the part, considering similar conditions of laser energy densities. It is also possible to determine the correlation between a microstructure and the laser strategy used, observing the patterns formed by the laser on the surface of the samples. Some samples were tested to measure their hardness and the result is comparable to conventionally processed 8YSZ. A relative density of 97 % was achieved without any post-treatments. Further investigations are still needed to understand deeper the effects of heat flow and diffusion, platform material, other laser parameters and strategies.

Funding

The project DOC-3D-printing has received funding from the European Union's Horizon 2020 research and innovation programme under the Marie Skłodowska-Curie grant agreement No 764935.

Data availability

The data that has been used is confidential.

Declaration of Competing Interest

The authors declare that they have no known competing financial interests or personal relationships that could have appeared to influence the work reported in this paper.

References

[1] D. Grossin, A. Montón, P. Navarrete-Segado, E. Özmen, G. Urruth, F. Maury, D. Maury, C. Frances, M. Tourbin, P. Lenormand, G. Bertrand, A review of additive manufacturing of ceramics by powder bed selective laser processing (sintering / melting): calcium phosphate, silicon carbide, zirconia, alumina, and their composites, Open Ceram. 5 (2021), 100073.
[2] E. Atzeni, A. Salmi, Economics of additive manufacturing for end-usable metal parts, Int. J. Adv. Manuf. Technol. 62 (2012) 1147–1155.
[3] M. Schröder, B. Falk, R. Schmitt, Evaluation of cost structures of additive manufacturing processes using a new business model, Procedia CIRP 30 (2015) 311–316.
[4] L. Ferrage, G. Bertrand, P. Lenormand, D. Grossin, B. Ben-Nissan, A review of the additive manufacturing (3DP) of bioceramics: alumina, zirconia (PSZ) and hydroxyapatite, J. Aust. Ceram. Soc. 53 (2017) 11–20.
[5] N.K. Tolochko, Yurii V. Khlopkov, Sergei E. Mozzharov, Michail B. Ignatiev, Tahar Laoui, Victor I. Titov, Absorptance of powder materials suitable for laser sintering, Rapid Prototyp. J. 6 (2000) 155–161.
[6] L. Ferrage, G. Bertrand, P. Lenormand, Dense yttria-stabilized zirconia obtained by direct selective laser sintering, Addit. Manuf. 21 (2018) 472–478.
[7] D.S. Almeida, C.R.M. Silva, M.C.A. Nono, C.A.A. Cairo, Thermal conductivity investigation of zirconia co-doped with yttria and niobia EB-PVD TBCs, Mater. Sci. Eng. A 443 (2007) 60–65.
[8] K. Tomida, T. Namikawa, Y. Yamazaki, Tensil test of corrugated 8 YSZ thin films for SOFC, Denki Kagaku 1961 (62) (1994) 1043–1047.
[9] J. Chevalier, What future for zirconia as a biomaterial? Biomaterials 27 (2006) 535–543.
[10] E.W. Leib, V. Ulla, R.M. Pasquarelli, J. Kus, C. Czaschke, N. Walter, R. Janssen, M. Müller, A. Schreyer, H. Weller, T. Vossmeyer, Synthesis and thermal stability of zirconia and yttria-stabilized zirconia microspheres, J. Colloid Interface Sci. 448 (2015) 582–592.
[11] Unknown author, The different forms of Zirconia. Zirconia 12–16, Elsevier, 1992.
[12] Ph. Bertrand, F. Bayle, C. Combe, P. Goeuriot, I. Smurov, Ceramic components manufacturing by selective laser sintering, Appl. Surf. Sci. 254 (2007) 989–992.
[13] Q. Liu, Y. Danlos, B. Song, B. Zhang, S. Yin, H. Liao, Effect of high-temperature preheating on the selective laser melting of yttria-stabilized zirconia ceramic, J. Mater. Process. Technol. 222 (2015) 61–74.
[14] E. Juste, F. Petit, V. Lardot, F. Cambier, Shaping of ceramic parts by selective laser melting of powder bed, J. Mater. Res. 29 (2014) 2086–2094.
[15] S. Chang, L. Li, L. Lu, J. Fuh, Selective laser sintering of porous silica enabled by carbon additive, Materials 10 (1313) (2017).
[16] K. Florio, S. Pfeiffer, M. Makowska, N. Casati, F. Verga, T. Graule, H. Van Swygenhoven, K. Wegener, An innovative selective laser melting process for hematite-doped aluminum oxide, Adv. Eng. Mater. 21 (2019), 1801352.
[17] M. Makowska, K. Florio, S. Pfeiffer, N. Casati, M. Vitterli, T. Graule, H. Van Swygenhoven, K. Wegener, Pre-processing of hematite-doped alumina granules for Selective Laser Melting, Ceram. Int. 45 (2019) 17014–17022.
[18] S. Pfeiffer, M. Makowska, K. Florio, D.F. Sanchez, F. Marone, X. Zhang, C. G. Aneziris, H. Van Swygenhoven, K. Wegener, T. Graule, Selective laser melting of thermal pre-treated metal oxide doped aluminum oxide granules, Open Ceram. 2 (2020), 100007.
[19] K. Florio, D. Puccio, D. Viganò, S. Pfeiffer, F. Verga, M. Grasso, B.M. Colosimo, T. Graule, K. Wegener, Process characterization and analysis of ceramic powder bed fusion, Int. J. Adv. Manuf. Technol. 117 (2021) 2105–2116.
[20] F. Verga, M. Borlaf, L. Conti, K. Florio, M. Vetterli, T. Graule, M. Schmid, K. Wegener, Laser-based powder bed fusion of alumina toughened zirconia, Addit. Manuf. 31 (2020), 100959.
[21] S.R. Jain, K.C. Adiga, V.R. Pai Verneker, A new approach to thermochemical calculations of condensed fuel-oxidizer mixtures, Combust. Flame 40 (1981) 71–79.
[22] C. Durmus, O.S. Ozgen, Experimental synthesis of granulated zirconia powders by spray dryer, Mater. Lett. 145 (2015) 243–246.
[23] T. Peng, C. Chen, Influence of energy density on energy demand and porosity of 316L stainless steel fabricated by selective laser melting, Int. J. Precis. Eng. Manuf. Green Technol. 5 (2018) 55–62.
[24] K.G. Prashanth, S. Scudino, T. Maity, J. Das, J. Eckert, Is the energy density a reliable parameter for materials synthesis by selective laser melting? Mater. Res. Lett. 5 (2017) 386–390.
[25] U. Scipioni Bertoli, A.J. Wolfer, M.J. Matthews, J.-P.R. Delplanque, J. M. Schoenung, On the limitations of Volumetric Energy Density as a design parameter for Selective Laser Melting, Mater. Des. 113 (2017) 331–340.
[26] L. Thijs, K. Kempen, J.-P. Kruth, J. Van Humbeeck, Fine-structured aluminium products with controllable texture by selective laser melting of pre-alloyed AlSi10Mg powder, Acta Mater. 61 (2013) 1809–1819.
[27] J. Suryawanshi, J. Prashanth, S. Scudino, J. Eckert, Om. Prakash, U. Ramamurty, Simultaneous enhancements of strength and toughness in an Al-12Si alloy synthesized using selective laser melting, Acta Mater. 115 (2016) 285–294.
[28] F. Shi, Y. Li, H. Wang, Q. Zhang, Fabrication of well-dispersive yttrium-stabilized cubic zirconia nanoparticles via vapor phase hydrolysis, Prog. Nat. Sci. 22 (2012) 15–20.
[29] H. Zhou, J. Li, D. Yi, L. Xiao, Effect of manganese oxide on the sintered properties of 8YSZ, Phys. Procedia 22 (2011) 14–19.
[30] R. Ge, Z. Liu, H. Chen, D. Zhang, T. Zhao, Wet-milling effect on the properties of ultrafine yttria-stabilized zirconia powders, Ceram. Int. 22 (1996) 123–130.
[31] G. Miao, W. Du, M. Moghadasi, Z. Pei, C. Ma, Ceramic binder jetting additive manufacturing: effects of granulation on properties of feedstock powder and printed and sintered parts, Addit. Manuf. 36 (2020), 101542.
[32] P. Luo, J. Zhang, Z. You, X. Ran, Y. Liu, S. Li, S. Li, Effect of TiO2 content on the microstructure and mechanical and wear properties of yttria-stabilized zirconia ceramics prepared by pressureless sintering, Mater. Res. Express 6 (2020), 125211.
[33] L. Qian, L. Yang, G. Li, W. Jiang, Z. Fan, Effect of nano-TiO2 on properties of 3 mol % yttria-stabilized zirconia ceramic via layered extrusion forming, J. Eur. Ceram. Soc. 40 (2020) 4539–4546.

[34] C.T. Shen, K.R. Lee, Y.P. Hsieh, S.W. Lee, J.K. Chang, S.C. Jang, C.J. Tseng, Effects of TiO2 and SDC addition on the properties of YSZ electrolyte, Int. J. Hydrogen Energy 44 (2019) 29426–29431.
[35] X. Lu, G. Li, Jin Y. Kim, K.D. Meinhardt, V.L. Sprenkle, Enhanced sintering of b''-Al2O3/YSZ with the sintering aids of TiO2 and MnO2, J. Powder Sources 295 (2015) 167–174, https://doi.org/10.1016/j.jpowsour.2015.06.147.
[36] G.R. Nazami, S. Sahoo, Influence of hatch spacing and laser spot overlapping on heat transfer during laser powder bed fusion of aluminum alloy, J. Laser Appl. 32 (2020), 042007.
[37] G. Dursun, S. Ibekwe, G. Li, P. Mensah, G. Joshi, D. Jerro, Influence of laser processing parameters on the surface characteristics of 316L stainless steel manufactured by selective laser melting, Mater. Today Proc. 26 (2020) 387–393.
[38] L. Ferrage, Elaboration d'un assemblage céramique-métal par fusion/frittage sélectif(ve) d'un lit de poudre à l'aide d'un laser Nd :YAG. Thesis dissertation, Université Toulouse III – Paul Sabatier, 2018.
[39] P. Navarrete-Segado, C. Frances, M. Tourbin, C. Tenailleau, B. Duployer, D. Grossin, Powder bed selective laser process (sintering/melting) applied to tailored calcium phosphate-based powders, Addit. Manuf. 50 (2022), 102542.